# 1,2H hyperfine spectroscopy and DFT modeling unveil the demethylmenasemiquinone binding mode to E. coli nitrate reductase A (NarGHI)

Maryam Seif Eddine, Frédéric Biaso, Julia Rendon, Eric Pilet, Bruno Guigliarelli, Axel Magalon, Stéphane Grimaldi

# $^{1,2}$H hyperfine spectroscopy and DFT modeling unveil the demethylmenasemiquinone binding mode to *E. coli* nitrate reductase A (NarGHI)

Maryam Seif Eddine, [a,1] Frédéric Biaso, [a] Julia Rendon, [a,2] Eric Pilet,[a] Bruno Guigliarelli, [a] Axel Magalon, [b] Stéphane Grimaldi [a,*]

[a] *Aix Marseille Univ, CNRS, BIP, Marseille, France*

[b] *Aix Marseille Univ, CNRS, LCB, Marseille, France*

[1] *Present address: Imperial College London, Department of Chemistry, Molecular Sciences Research Hub, W12 0BZ, London, UK*

[2] *Present address: Univ. Grenoble Alpes, CEA, Department of the Interfaces for Energy, Health and Environment, Laboratoire SYMMES, Grenoble, France*

[*] Correspondence to: S. Grimaldi, Aix Marseille University, CNRS, Bioenergetics and Protein Engineering (BIP UMR7281), 31 chemin Joseph Aiguier, CS70071, 13402 Marseille cedex 09, France.

E-mail address: stephane.grimaldi@univ-amu.fr

**Keywords**

Bioenergetics • Quinones • HYSCORE • Metalloenzyme • Electron Transfer

**Abbreviations**

(b)RC, (bacterial) reaction center ; Cw, continuous wave; $E'_{m,7}$, midpoint redox potential at pH = 7; DFT, density functional theory ; (D)MK, (D)MSK, (D)$MKH_2$, (demethyl)menaquinone, (demethyl)menasemiquinone, (demethyl)menaquinol; (D)$MSK_D$, $USQ_D$, (demethyl)menasemiquinone and ubisemiquinone formed at the quinol oxidation site ($Q_D$) from *Ec*NarGHI, respectively; *Ec*NarGHI, membrane-bound nitrate reductase from *Escherichia coli*; ESEEM, electron spin echo envelope modulation; hf(c)(c)(s), hyperfine (coupling) (constant)(s); hfi, hyperfine interaction; EPR, electron paramagnetic resonance; HYSCORE, hyperfine sublevel correlation; IMVs, inner membrane vesicles; nq(cc), nuclear quadrupole (coupling constant) ; nqi, nuclear quadrupole interaction; Q, SQ, $QH_2$, quinone, semiquinone, quinol; SOMO, singly occupied molecular orbital.

**Abstract**

The quinol oxidation site $Q_D$ in *E. coli* respiratory nitrate reductase A (*Ec*NarGHI) reacts with the three isoprenoid quinones naturally synthesized by the bacterium, i.e. ubiquinones (UQ), menaquinones (MK) and demethylmenaquinones (DMK). The binding mode of the demethylmenasemiquinone (DMSK) intermediate to the *Ec*NarGHI $Q_D$ quinol oxidation site is analyzed in detail using $^{1,2}$H hyperfine (hf) spectroscopy in combination with $H_2O/D_2O$ exchange experiments and DFT modeling, and compared to the menasemiquinone one bound to the $Q_D$ site ($MSK_D$) previously studied by us. $DMSK_D$ and $MSK_D$ are shown to bind in a similar and strongly asymmetric manner through a short (~1.7 Å) H-bond. The origin of the specific hf pattern resolved on the $DMSK_D$ field-swept EPR spectrum is unambiguously ascribed to slightly inequivalent contributions from two β-methylene protons of the isoprenoid side chain. DFT calculations show that their large isotropic hf coupling constants ($A_{iso}$ ~ 12 and 15 MHz) are consistent with both (i) a specific highly asymmetric binding mode of $DMSK_D$ and (ii) a near in-plane orientation of its isoprenyl chain at Cβ relative to the aromatic ring, which differs by ~ 90° to that predicted for free or NarGHI-bound MSK. Our results provide new insights into how the conformation and the redox properties of different natural quinones are selectively fine-tuned by the protein environment at a single Q site. Such a fine-tuning most likely contributes to render NarGHI as an efficient and flexible respiratory enzyme to be used upon rapid variations of the Q-pool content.

## 1. Introduction

Isoprenoid quinones are lipophilic electron mediators which play key roles in bioenergetics processes leading to efficient harvesting of environmental energy and its conversion into a transmembrane chemiosmotic potential. While they all bear a ring moiety with two oxygen atoms at positions 1 and 4, their chemical structure and electrochemical properties can differ significantly. The vast majority of biological isoprenoid quinones belong to either the low-potential naphthoquinones, e.g. phylloquinones (PhQ or vitamin $K_1$) and menaquinone (MK or vitamin $K_2$), or to the higher potential benzoquinones, e.g. ubiquinone (UQ) and plastoquinone (PQ) (Fig. 1) [1]. The crucial role of isoprenoid quinones in bioenergetics relies mainly on (i) their soluble character in lipid bilayers conferred by their apolar hydrophobic side chain which can vary in length, in degree of saturation and in the presence of additional groups, and (ii) on the redox properties of their aromatic ring which can easily and reversibly oscillate under physiological conditions between three different oxidation states with different protonation levels: the oxidized deprotonated quinone state (Q), the intermediate semiquinone (SQ) form which can be anionic ($SQ^{\bullet -}$) or neutral ($SQH^{\bullet}$), and the fully reduced and protonated quinol state ($QH_2$).

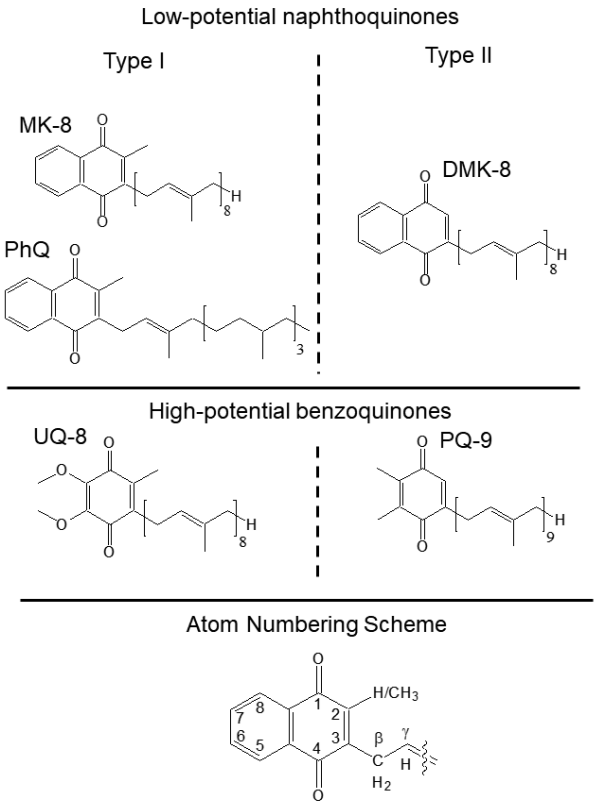

**Fig. 1.** Chemical structures of some naturally occurring isoprenoid low- and high-potential quinones. The type I and type II classification is based on the nature of the C2 substituting group, namely a methyl group for type I and a hydrogen atom for type II [2]. The atom numbering scheme used in the text is shown at the bottom. (D)MK-8, (demethyl)menaquinone-8, PhQ, phylloquinone, UQ-8, ubiquinone-8, PQ-9, plastoquinone-9. The digit indicates the number of prenyl units which may vary in a given organism or between different species. The α-protons are directly bound to the aromatic rings, and the β-protons are found within the methyl group and the first $CH_2$ group of the quinone prenyl (or phytyl for PhQ) chain.

Isoprenoid quinones interact with bioenergetic complexes within well-defined protein sites (called Q sites) where they transiently bind and exchange with the Q-pool, or act as permanently bound cofactors possibly involved in intramolecular electron transfer and proton exchange. Several studies on photosynthetic and respiratory complexes have shown that the (electro)chemical properties of the protein-bound quinones and therefore the reactivity towards quinones can be drastically modulated in a Q site, hence contributing to define the electron transfer directionality in a particular enzyme or its specificity towards quinones [3-6].

The ability of some facultative anaerobes such as *E. coli* to synthesize both low potential (i.e. MK with $E'_{m,7}$ MK/$MKH_2$ = -70 ± 10 mV) and high potential quinones (i.e. UQ with $E'_{m,7}$ UQ/$UQH_2$ = + 100 ± 10 mV) [1] opens up the possibility to investigate *in vivo* the specificity of quinone utilization by respiratory complexes [7]. In this context, the respiratory nitrate reductase complex NarGHI from *E. coli* (*Ec*NarGHI) is an excellent model to address this issue. *Ec*NarGHI is a membrane-bound heterotrimeric complex which couples the oxidation of quinols at a periplasmically-oriented Q site ($Q_D$) [8] to the cytoplasmic two-electron reduction of nitrate into nitrite [5, 9, 10]. *Ec*NarGHI turnover induces a net translocation of protons across the membrane which contributes to maintaining the transmembrane proton gradient that drives, for instance, ATP synthesis. The NarG catalytic subunit holds the Mo-*bis*Pyranopterin Guanosine Dinucleotide cofactor [11] and a FeS cluster [10, 12, 13]. The electron transfer subunit NarH harbors four FeS clusters [9, 14]. Finally, the cytoplasmically exposed NarGH subunits are connected to the membrane-integral NarI, which has two *b*-type hemes termed $b_D$ and $b_P$ according to their respective distal and proximal positions with respect to the nitrate reducing site [10, 15, 16]. The metal cofactors form a chain of electron transfer relays from the quinol oxidation site $Q_D$ in NarI to the molybdenum cofactor in NarG.

*Ec*NarGHI has been shown to react with the three quinones synthesized by the bacterium, namely MK, UQ and demethylmenaquinone (DMK) [17-19]. DMK differs from MK by the lack of the methyl group at the C2 position of the quinone ring and by its ~ 60 mV higher redox potential ($E'_{m,7}$ DMK/$DMKH_2$ = +36 [20] or -7 mV [21]) (Fig. 1). Using EPR-monitored redox titrations on *E. coli* inner membrane vesicles (IMVs) enriched in NarGHI, we have previously shown that the *Ec*NarGHI $Q_D$ site stabilizes the semiquinone intermediate of each of the three endogenous quinones. Noteworthy, a specific hf interaction with a $^{14}N$ nucleus was similarly detected to each of the three corresponding protein-bound radicals using HYSCORE spectroscopy [19, 22, 23]. Based on multifrequency $^{14,15}N$ ESEEM/HYSCORE measurements [23], site-directed mutagenesis studies [22, 24] and selective $^{15}N$ labeling [25], this interacting nucleus has been ascribed to the $N_\delta$ imidazole nitrogen of the heme $b_D$ axial ligand His66. Combining the use of $H_2O/^2H_2O$ exchange experiments, selective $^2H$ labeling of the ring methyl protons and $^{1,2}H$ hyperfine spectroscopies, we have shown that $MSK_D$ is stabilized thanks to a short in-plane H-bond to the quinone oxygen O1, leading to a highly asymmetric distribution of the electron spin density over the semiquinone ring in comparison with the unbound species [25, 26].

Intriguingly, EPR-monitored redox titrations indicated that, in contrast to MSK and USQ [22, 27], the two-electron midpoint potential of *Ec*NarGHI-bound DMK is decreased by at least 30 mV with respect to that of the unbound species [25]. This shift likely results from a redox-dependent differential binding of DMK at the $Q_D$ site corresponding to a ~10 fold tighter binding of DMK than $DMKH_2$ to this site. In addition, in contrast to $USQ_D$ and $MSK_D$, the $DMSK_D$ EPR signal exhibits a resolved hf structure from one or several nearby non exchangeable protons [19] whose origin was unclear. Its linewidth has been shown to decrease upon $H_2O/^2H_2O$ exchange, revealing the existence of at least one exchangeable proton weakly coupled to $DMSK_D$ [25].

To fully resolve the $DMSK_D$ electronic structure and address the role of the C2 substituent on the naphthoquinone ring in binding to the *Ec*NarGHI $Q_D$ site, we performed a detailed spectroscopic analysis of $DMSK_D$ using $^{1,2}H$ hyperfine pulsed EPR spectroscopy in combination with $H_2O/^2H_2O$ exchange experiments and DFT modeling. Our results show that, in spite of a conserved asymmetric binding mode through a short H-bond, both $DMSK_D$ and $MSK_D$ exhibit markedly different orientations of their isoprenyl side-chain. This sheds new light on how a single Q site enables the binding of different quinones and modulate their structural and redox properties.

## 2. Material and methods

### *2.1. Sample preparations*

NarGHI was expressed in an *E. coli* nitrate reductase-deficient strain JCB4023*ubiE* (RK4353, *ΔnapA-B, narG*::*ery, ΔnarZ*::*Ω*, $Spc^R$, *ΔubiE*::*Kan*$^R$) [19, 28] which contains demethylmenaquinone as sole respiratory quinone. pVA700 plasmid ($Amp^R$) [14], which encodes for the *narGHJI* operon under control of the tac promoter, was used in all experiments. Cells were grown in Terrific Broth under semi-anaerobic conditions at 37 °C as described in [19, 24] with ampicillin (100 $\mu g.ml^{-1}$) and spectinomycin (50 $\mu g.ml^{-1}$) included in the growth medium.

Purified *E. coli* NarGHI-enriched inner membrane vesicles (IMVs) were used for this study, allowing to maintain an unmodified lipid environment and to study the interaction of NarGHI with its endogenous demethylmenaquinol substrate. For this purpose, purified *E. coli* NarGHI-enriched IMVs were isolated by differential centrifugation and sucrose gradient steps as described in [24] using a buffer containing 100 mM MOPS and 5 mM EDTA at pH 7.5. Deuterium-exchanged samples were prepared using the same membrane extraction protocol with a buffer containing $^2H_2O$ (99.9 % atom $^2H$) instead of $^1H_2O$. The functionality of NarGHI in our samples was confirmed spectrophotometrically by measuring the quinol:nitrate oxidoreductase activity. Stabilization of the semiquinone at the $Q_D$ site was achieved through redox titrations under the same conditions as those described in [19, 24, 27] except that samples were prepared in a glove box. They were redox poised at a potential allowing to maximize the DMSK concentration with respect to the two other redox species (~ - 60 to -90 mV) [19]. Redox potentials are given in the text with respect to the standard hydrogen electrode.

### *2.2. EPR and HYSCORE spectroscopy*

The instrumentation for X- and Q-band CW EPR measurements was previously described [24]. The instrumentation, pulse sequences, and spectral processing for X-band 1D 4-pulse ESEEM ($\pi/2$-$\tau$-$\pi/2$-t-$\pi$-t-$\pi/2$-$\tau$-echo) and 2D 4-pulse ESEEM (HYSCORE) ($\pi/2$-$\tau$-$\pi/2$-$t_1$-$\pi$-$t_2$-$\pi/2$-$\tau$-echo) were also as described [26]. Spectral simulations were carried out using the EasySpin package (release 5.01.1) under Matlab (The MathWorks, Inc., US) [29]. Simulations of $^{1,2}H$ HYSCORE spectra were carried out assuming axial hfi tensors. Principal axes of hf tensors were all assumed to be collinear with the g-tensor principal axes unless explicitly stipulated otherwise.

*2.3. Hyperfine and nuclear quadrupole interactions*

A hfc between a S = ½ radical and a nucleus with nuclear spin value I consists in general of (i) the isotropic contribution $A_{iso} = 2\mu_0 g_e g_n \beta_e \beta_n |\psi_0(0)|^2/3h$ where $|\psi_0(0)|^2$ is the electron spin density at the nucleus, $g_e$ and $g_n$ are electron and nuclear g-factors, respectively, $\beta_e$ and $\beta_n$ are Bohr and nuclear magnetons, respectively, h is Planck's constant, and (ii) the anisotropic contribution described by the traceless dipolar coupling tensor $\underline{\mathbf{T}}$. In most cases, $\underline{\mathbf{T}}$ can be assumed to be axial, with principal values (–T, –T, 2T).

The hfccs of different isotopes of the same element are proportional to a very good approximation to the corresponding $g_n$ values. In this study, the direct and simultaneous determination of $A_{iso}$ and T of the protons interacting with DMSK were derived from the analysis of $^1$H HYSCORE cross-peak contours as described in the Supporting Information [30].

A $^2$H nucleus has a quadrupole moment which interacts with the electric field gradient (EFG) at the nucleus. The components of the EFG tensor are defined in its principal axis system and ordered according to $|q_{ZZ}| \geq |q_{YY}| \geq |q_{XX}|$. This traceless tensor can then be fully described by only two parameters: (i) the $^2$H nuclear quadrupole coupling constant $\kappa = |e^2 q_{ZZ} Q/h|$, where e is the charge of an electron, Q is the $^2$H nuclear electric quadrupole moment, (ii) the asymmetry parameter $\eta = |q_{YY}-q_{XX}/q_{ZZ}|$. $\kappa$ is a measure of the strength of the interaction between the nuclear quadrupole moment and the EFG at the $^2$H nucleus site due to anisotropic charge distribution around the nucleus whereas $\eta$ is a measure of the deviation of this distribution from axial symmetry. Thus, the EFG is related to the specific binding geometry. Its components can, therefore, be used to obtain detailed information on hydrogen bonds. In this study, parameters $\kappa$ and $\eta$ of the $^2$H nucleus interacting with $DMSK_D$ were estimated by simulating X-band $^2$H HYSCORE spectra.

*2.4. DFT calculations*

All calculations have been performed with Orca 3.0 quantum chemistry package [31] at a DFT level of theory, using the B3LYP hybrid functional (the Becke's three parameters hybrid exchange functional with 20% of Hartree-Fock admixture and the Lee-Yang-Parr non local correlation functional). A restricted geometry optimization has been performed *in vacuo* on each model with the def2-SVP basis set [32, 33]. The resolution of identity with the appropriate auxiliary basis sets was used to accelerate the calculations [34]. The optimized

structures have then been used as input for electronic and magnetic properties calculations, using the EPR-II basis set [35] and employing the conductor-like screening model COSMO [36] with a dielectric constant ε = 4.0 to replicate electrostatic effects of the protein surrounding. $^{1}$H hfi and $^{2}$H nqi coupling constants of the methyl group were calculated by averaging the raw matrices corresponding to the three positions of the methyl protons and the eigenvalues and eigenvectors were determined.

## 3. Results and discussion

### *3.1. Field swept Electron Spin Echo (ESE) EPR spectra of DMSK*

To specifically study the interaction of *Ec*NarGHI with its natural DMK substrate, NarGHI-enriched IMVs were purified from an *E. coli ubiE*$^{-}$ strain containing DMK as its sole respiratory quinone. The sample was titrated and redox poised to stabilize the maximal amount of DMSK, and studied by EPR methods at 90 K. At this temperature, the radical can be specifically probed without spectral contamination from other faster relaxing paramagnetic centers such as EPR-active cofactors in *Ec*NarGHI [19]. X-band field swept ESE spectra of NarGHI-enriched IMVs recorded at 90 K from samples prepared either in $H_2O$ (solid line) or in $^{2}H_2O$ (dotted line) are shown in Fig. 2. The EPR signal is characterized by an average g-value $g_{av}$ ~ 2.0045. This signal is not present in NarGHI-deficient IMVs prepared and titrated in similar conditions [19]. The characteristic structure of $DMSK_D$ is best resolved in the ESE spectrum recorded using the $^{2}H_2O$-exchanged sample due to the decrease of the linewidth upon replacement of $H_2O$ by $^{2}H_2O$ [19]. This decrease, which results from downscaling of hyperfine coupling constants (hfccs) of exchangeable $^{2}$H nuclei by a factor of ~ 6.5 compared to the $^{1}$H one's, indicates that at least one nearby exchangeable proton is coupled to the radical [19]. In the following, spectral resolution was further increased by using 2D pulsed hyperfine spectroscopy.

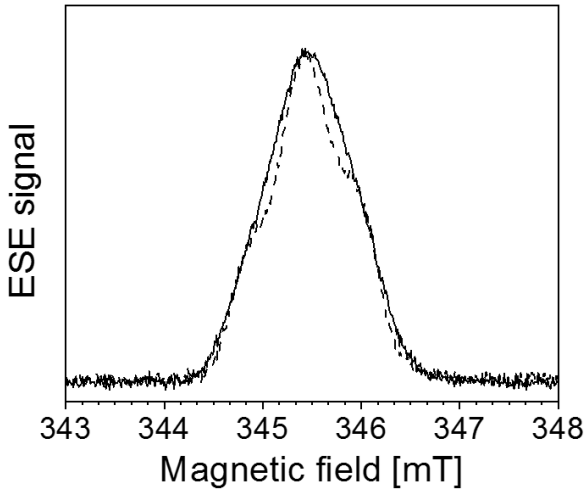


**Fig. 2.** Field swept ESE spectra of NarGHI-bound DMSK prepared in $H_2O$ (solid line) and $^2H_2O$ (dotted line). Microwave frequency, 9.700 GHz ($H_2O$), 9.686 GHz ($^2H_2O$). A magnetic field offset of -4.5 G was applied to the spectrum measured in $^2H_2O$. Spectra are normalized to the same amplitude.

*3.2. Analysis of $^1H$ resonances in HYSCORE spectra of DMSK in $H_2O$ or $^2H_2O$ buffer*

To provide detailed insights into the $DMSK_D$ electronic structure and accurate information about its proton environment, HYSCORE experiments were performed at 90 K using the *Ec*NarGHI samples studied in previous section. Fig. 3A shows a representative $^1H$ HYSCORE spectrum of $DMSK_D$ prepared in $H_2O$ buffer. It has been recorded with $\tau$ = 204 ns to suppress the strong diagonal peak at $\nu(^1H)$ = 14.7 MHz contributed by matrix protons. Five pairs of cross-features located symmetrically relative to the diagonal can be distinguished in this spectrum. They are designated 1-5 in Fig. 3A and arise from protons that are magnetically coupled with the unpaired electron spin of $DMSK_D$. Among them, ridges 5, 5' exhibit the largest hf splitting estimated to ~ 15 MHz by measuring the distance between their maxima. They appear therefore well separated from the others which are contributed by protons with hfccs smaller than ~ 6 MHz. Notably, the ~ 15 MHz splitting is nearly three times larger than the largest one previously detected on the corresponding $^1H$ HYSCORE spectrum of $MSK_D$ and assigned to the three equivalent methyl protons with $A_{iso}$ ~ 5.5 MHz [25, 26]. Cross-ridges 3-3' possess the most extended anisotropic contour, with the largest deviation from the diagonal, whereas cross-peaks 4-4' deviate significantly from the normal to the diagonal. These two features indicate a significant anisotropic component of the corresponding hfi tensor(s). Cross-peaks 2-2' and 4-4' partially overlap. Contours 1-1' and 2-2' are

approximately normal to the diagonal, suggesting a smaller anisotropic component of the corresponding $^{1}$H hfi tensors. To discriminate cross-features arising from exchangeable or non-exchangeable protons, HYSCORE measurements were carried out on the sample prepared in $^{2}H_2O$ buffer using similar conditions to those used for the sample prepared in $H_2O$ (Fig. 3B). Cross-peaks 3-3' and 4-4' completely disappear in the $DMSK_D$ $^{1}$H HYSCORE spectrum of the sample prepared in $^{2}H_2O$ buffer. This shows that they arise from at least one exchangeable proton, in consistency with the decrease of the linewidth observed in the field-swept EPR spectra upon $H_2O/^{2}H_2O$ buffer exchange. In contrast, the other cross-peaks are not affected by buffer exchange, indicating that they are produced by nonexchangeable protons. No other feature than those discussed above were detected in $^{1}$H HYSCORE spectra recorded using other $\tau$ values.

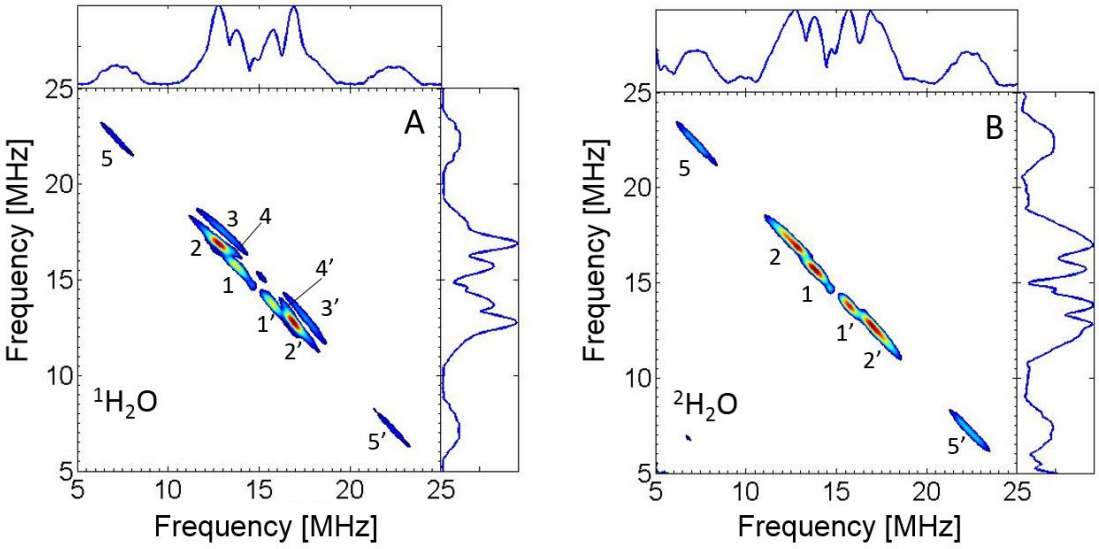


**Fig. 3.** $^{1}$H HYSCORE spectra of $DMSK_D$ in $H_2O$ (A) or in $^{2}H_2O$ (B). Microwave frequency, 9.6944 GHz (A) and 9.7045 GHz (B); magnetic field, 345.2 mT (A) and 345.9 mT (B). Other experimental parameters are as given in Material and methods, time between first and second pulses $\tau$ = 204 ns.

$^{1}$H HYSCORE spectra were quantitatively analyzed using the square frequency plot to assess the number of coupled protons and determine their respective hyperfine characteristics [30]. The $\nu_\alpha^2$ versus $\nu_\beta^2$ plot of the cross-features analyzed from the $DMSK_D$ $^{1}$H HYSCORE spectra shown in Fig. 3 is depicted in Fig. 4 together with linear regressions of ridges 1-5 and assuming axial symmetry for all proton hyperfine interaction (hfi) tensors. The corresponding slopes and intercepts are given in Table S1 with the two possible sets of ($A_{iso}$, T) that satisfy

Eq. S2 and S3. The results indicate that ridges 1-1' and 2-2' arise from at least two distinct non exchangeable protons, hereafter referred to as $H_A$ and $H_B$, respectively, whereas 3-3' and 4-4' are the sub-ridges of cross-features belonging to a single additional exchangeable proton named $H_C$ characterized by an anisotropic contribution $|T(H_C)| \sim 5.6$ MHz. This value is consistent with the one calculated from the shift of the single sum combination line from $2\nu_I(^1H)$ measured in four-pulse $^1H$ ESEEM spectra of $DMSK_D$ prepared in $H_2O$ (see supplementary information and Fig. S1). In contrast to $H_A$ and $H_B$, selection of the right ($A_{iso}$, T) for proton $H_C$ from the two alternatives has been achieved based on numerical simulations of HYSCORE spectra. Indeed, the experimental relative intensities of ridges 3-3' and 4-4' can only be well reproduced using $A_{iso} = \mp 0.2$ MHz and $T = \pm 5.8$ MHz (Fig. 5A and Table 1).

A peculiar feature of $^1H$ HYSCORE spectra of $DMSK_D$ prepared either in $H_2O$ or in $^2H_2O$ is the presence of cross peaks 5-5' indicating that these features arise from at least one non exchangeable proton strongly coupled to the radical (Fig. 3). In contrast to the other HYSCORE features, the points measured along the 5-5' ridges do not align on a straight line in the square frequency plot, rendering the simple analysis presented above not satisfactorily applicable. However, ridges 5-5' are well accounted for by a linear regression assuming that they are due to partially overlapping cross-features originating from two protons with distinct axially symmetric hfi tensors and that each of them mainly contributes to opposite sides (referred to $5_A$-$5'_A$ and $5_B$-$5'_B$ in Fig. 4) of the same ridge. Using this approach, the anisotropic components of the hf tensors of these two protons (hereafter referred to as $H_D$ and $H_E$) are found to be similar, namely $|T| \sim 2.0$-$2.1$ MHz while their isotropic components are slightly different, i.e. $|A_{iso}|$ ($H_D$) = 12 or 14 MHz, and $|A_{iso}|$ ($H_E$) = 15 or 17 MHz (Table S1).

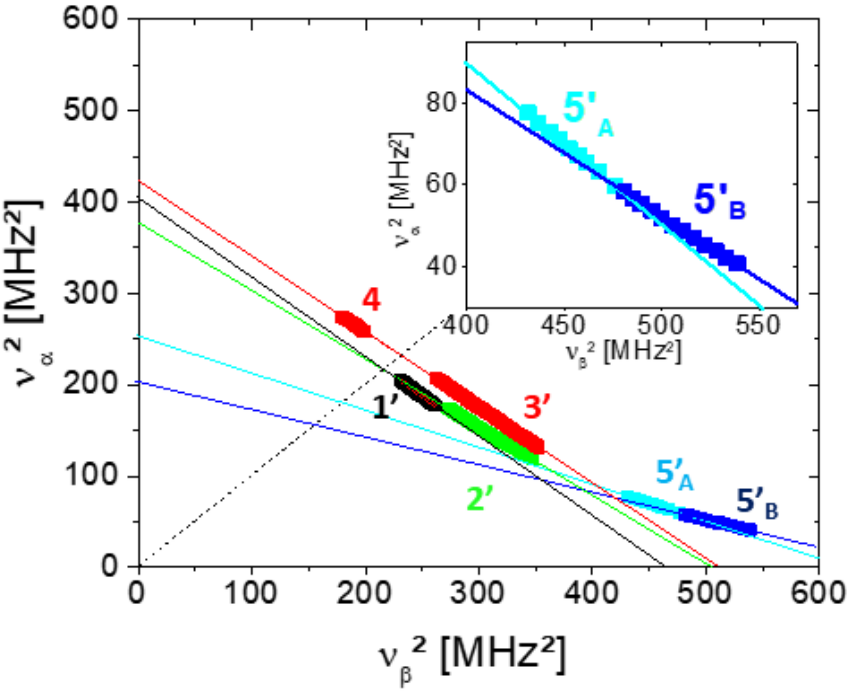


**Fig. 4.** Plot of cross-peaks detected in $^1$H HYSCORE spectra of DMSK in the $\nu_\alpha^2$ *versus* $\nu_\beta^2$ coordinate system. Straight lines show the linear fit of plotted data points. The dashed line is defined by $\nu_\alpha^2 = \nu_\beta^2$ and corresponds to the diagonal in the (+, +) quadrant of HYSCORE spectra. The lowermost contours were used to measure the coordinates of arbitrary points along the ridge of each proton cross-peak in HYSCORE spectra of $DMSK_D$ in $H_2O$ (3', 4) or $^2H_2O$ (1', 2', 5').

*3.3. Characterization of the exchangeable deuteron by $^2$H HYSCORE*

Further details concerning exchangeable protons coupled to $DMSK_D$ were obtained through the use of $^2$H HYSCORE spectroscopy. Given that the largest exchangeable proton splitting in the $DMSK_D$ HYSCORE spectra measured at different $\tau$ values is ~ 6 MHz and that $^2$H nuclei give rise to weak quadrupole splittings (typically a few tenths of MHz) [26, 37], a splitting not greater than 1 MHz is predicted in $DMSK_D$ $^2$H HYSCORE spectra. However, this feature is expected to be hardly detectable because of the intense and broad diagonal peak at $\nu_I(^2H)$ ~ 2.3 MHz arising from weakly coupled matrix $^2$H which dominates ESEEM/HYSCORE spectra of $^2H_2O$ exchanged protein samples [26, 38]. To suppress this intense signal, a HYSCORE spectrum of $DMSK_D$ prepared in $^2H_2O$ buffer has been measured using a $\tau$-value of 416 ns and is shown in Fig. 5B. It is compared to the corresponding spectrum of $MSK_D$ measured using similar conditions (Fig. 5C). Complete suppression of the peak at $\nu_I(^2H)$ ~ 2.3 MHz allows to resolve croissant-shaped cross peaks positioned

symmetrically around $\nu_I(^2H)$ which are very similar for the two radicals. This peculiar shape for a powder HYSCORE spectrum of a (S = ½, I = 1) spin coupled system is well simulated by downscaling for $^2H$ nucleus the $H_C$ hf parameters obtained from analysis of the $^1H$ HYSCORE spectra, assuming that a single $^2H$ nucleus contributes (Fig. 5B). In addition, our numerical simulations indicated that the anisotropic hfi is mainly responsible for the elongation of the ridges perpendicularly to the diagonal (not shown) whereas the nqi is known to induce a splitting of the ridges parallel to the diagonal [39, 40], allowing these two contributions to be well distinguished from each other. Whereas the simulated spectrum is very sensitive to the magnitude of the nqcc κ, variations of the asymmetry parameter η in the [0, 1] range have negligible effects. Therefore, a value of $\kappa$ ($H_C$) = 0.17 ± 0.02 MHz can be estimated (Table 1). This value is consistent with that determined from analysis of the $DMSK_D$ Q-band $^2H$ Mims ENDOR spectrum measured at ~ 34 GHz (Fig. S2). Eventually, variations of the relative angle between the unique axes of hyperfine and nuclear quadrupole tensors have a modest effect on the simulated spectrum. This angle is therefore estimated to 0° ± 25°. Consequently, hyperfine and quadrupole tensors were assumed to be collinear in the simulations shown in Figure 5B and 5C.

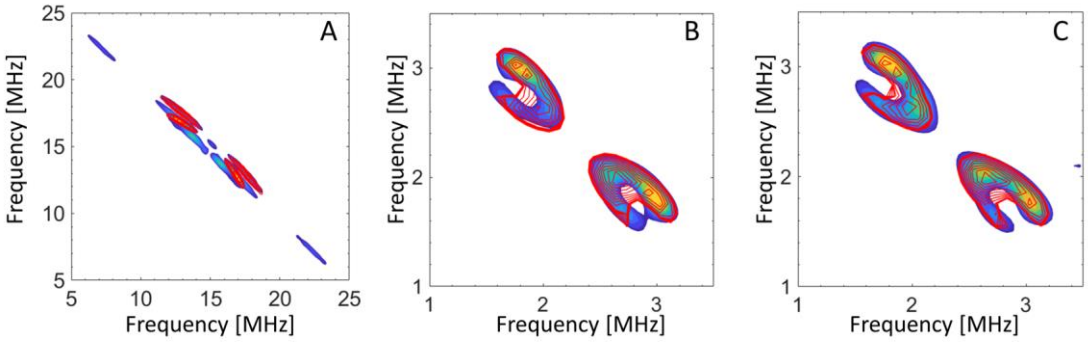


**Fig. 5.** Contour plot of experimental and simulated (red contours) HYSCORE spectra from the exchangeable $^1H$ (A) or $^2H$ (B, C) coupled to $DMSK_D$ (A,B) or $MSK_D$ (C) in *Ec*NarGHI prepared in $H_2O$ (A) and in $^2H_2O$ buffer (B, C). Simulation parameters are given in Table 1, and rescaled for $^2H$ nuclei when relevant. Other experimental parameters are: microwave frequency, 9.691 GHz (A), 9.686 GHz (B) and 9.693 GHz (B), τ-value, 204 ns (A) and 416 ns (B, C).

**Table 1**

$^{1}$H hyperfine and $^{2}$H nuclear quadrupole tensors of the exchangeable proton/deuteron coupled to $DMSK_D$ used for the simulation of $^{1}$H and $^{2}$H HYSCORE spectra. $^{1}$H hyperfine tensors were initially derived from linear regression of $^{1}$H HYSCORE spectra in square frequency plot. Selection of the set of ($A_{iso,}$ T) (Table S1) and evaluation of errors are based on numerical simulations while the signs of the couplings are selected according to DFT calculations. g-, hfi- and nqi tensors are assumed to be collinear. $^{2}$H nuclear quadrupole tensors are derived from simulations of $^{2}$H HYSCORE (Fig. 5) and Q-band $^{2}$H Mims ENDOR spectra (Fig. S2).

| Semiquinone species | $^{1}$H ($A_{iso}$, T) [MHz] | $^{2}$H ($\kappa$ [MHz],$\eta$) | References |
|---|---|---|---|
| $DMSK_D$ | -0.20 ± 0.06, 5.8 ± 0.1 | 0.17 ± 0.02, 0.2 | This work |
| $MSK_D$ | +0.06, 5.73 | 0.176, 0.2 | [25], [26] |

*3.4. The exchangeable proton coupled to $DMSK_D$ is involved in a short hydrogen bond to the radical*

Interestingly, comparative analysis of the $^{1,2}$H HYSCORE, four-pulse ESEEM and Q-band $^{2}$H Mims ENDOR spectra measured on $DMSK_D$ and $MSK_D$ reveals similar hfi and nqi characteristics for the detected exchangeable $^{1,2}$H nucleus ($H_C$) coupled to the two protein-bound radical intermediates (Table 1). On the basis of its hf characteristics, this exchangeable proton is assigned to a proton involved in H-bonding to one of the quinone carbonyl oxygens [26]. This proton combines both an almost zero $A_{iso}$ value and a relatively large |T| value (|T| ~ 5.6 MHz) for a proton H-bonded to a protein-bound semiquinone. A small $A_{iso}$ is expected when the H-bond lies in the quinone ring plane due to small overlap between the hydrogen 1s orbital and the oxygen 2*pz* orbital forming part of the semiquinone SOMO. In addition, the large |T| value of $H_C$ is predicted to account for a short hydrogen bond length with substantial covalent character. In this context, DFT calculations have shown that the H-bond length $r_{O-H}$ can be more reliably evaluated from the nqcc $\kappa$ of the corresponding substituted $^{2}$H using the following empirical relation [41]:

$$\kappa = a - b/r^{3}_{O-H} \qquad \text{(Eq. 1)}$$

where *a* and *b* are empirical parameters. The value $\kappa$ = 0.17 ± 0.02 MHz determined for $DMSK_D$ is similar to that obtained for $MSK_D$, confirming a similar hydrogen bond geometry of both radical species. A distance $r_{O-H}$ ~ 1.6 ± 0.1 Å can be estimated using Eq. 1, *a* = 319 kHz and *b* = 607 kHz·Å$^3$ [42]. This value is in the range of short hydrogen bonds for

biological systems. For instance, it is similar to that formed from the carbonyl oxygen O4 of the ubisemiquinone $Q_A^{\cdot-}$ in reaction centers from *Rhodobacter sphaeroides* R-26 to the imidazole nitrogen $N_\delta$ of His M219 ($r_{O\text{-}H}$ = 1.60 ± 0. 04 Å [42]. In addition, $^{14}$N HYSCORE spectroscopy has revealed a similar through-bond interaction of both $MSK_D$ and $DMSK_D$ with a nitrogen nucleus that, in the case of $MSK_D$, has been unambiguously assigned to the $N_\delta$ imidazole nitrogen of the heme $b_D$ axial ligand His66 [22, 23, 25]. Therefore, the exchangeable proton $H_C$ coupled to $DMSK_D$ is similarly attributed to a H-bond between one of the SQ oxygen atoms and this nitrogen atom.

*3.5. Assignment of $^1$H hyperfine couplings to $DMSK_D$ by DFT modeling*

A remarkable characteristic of $DMSK_D$ $^1$H HYSCORE spectra is the detection of cross peaks associated with unusually strong hf couplings arising from two non-exchangeable protons ($H_D$ and $H_E$). Notably, the isotropic hfcc of $H_E$ (i.e. ~ 16 MHz) is the largest one measured so far for a protein-bound semiquinone [43]. Importantly, spectral simulations (Fig. 6) show that the resolved hf structures detected on the cw X- and Q-band EPR spectra of $DMSK_D$ which are best seen in samples prepared in $^2H_2O$ are well accounted for by the contribution of protons $H_D$ and $H_E$ using the hfc tensors given in Table 2 derived from analysis of HYSCORE spectra (see Table S1 in Supplementary information).

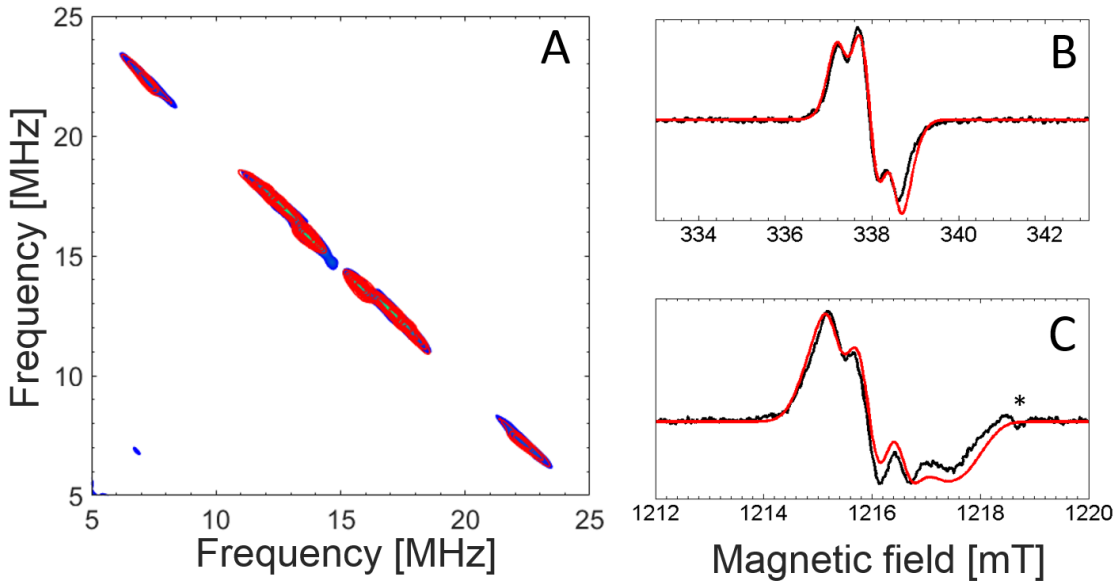

**Fig. 6.** A) Experimental and simulated (red contour plot) HYSCORE cross features of $DMSK_D$ in $^2H_2O$ buffer. B) Experimental (black solid line) and simulated (red dotted line) continuous wave EPR spectra of $DMSK_D$ in $^2H_2O$ measured at X- (B) and Q-band (C) frequencies. Simulations have been performed by considering the contributions of $H_A$, $H_B$, $H_D$ and $H_E$ with individual hfccs as given in Table 2. Experimental conditions: redox potential, -65 mV (A,B) and -70 mV (C), temperature, 60 K (B) and 150 K (C), microwave frequency, 9.482 GHz (B) and 34.122 GHz (C), microwave power, 0.1 mW (B) and 5 μW (C), modulation amplitude, 0.3 mT, modulation frequency, 100 kHz. The signal indicated by an asterisk in Fig. 6C is due to paramagnetic impurities in the Q-band resonator. Experimental spectrum in A) corresponds to that shown in Fig. 3B.

To identify the origin of the hf couplings, we assume that $DMSK_D$ and $MSK_D$ display a similar strongly asymmetric binding mode to NarGHI. Indeed, this assumption is based on the detection of similar hf and nq characteristics for the single exchangeable $^{1,2}H$ nucleus and of the $^{14}N$ nucleus coupled to $DMSK_D$ and $MSK_D$. In our previous work on $MSK_D$, these nuclei were shown to be involved in a short hydrogen bond to the quinone carbonyl oxygen O1 which induces a strong decrease (~ 30 %) of the spin density on the Cα at the 2-position in comparison to a symmetrical hydrogen bonding situation to both carbonyl oxygens [25, 26, 44]. This model was supported by DFT calculations performed on a simple molecular model referred to as Im-MSK involving a deprotonated MSK hydrogen bonded via its carbonyl oxygen O1 to the $N_\delta$ of an imidazole ring, with an isoprenoid chain truncated after the fourth carbon atom. Structural parameters inherent to this simple model were chosen to be consistent with available spectroscopic and crystallographic data. These include an O1-H distance $r_{O\text{-}H}$ of 1.7 Å between the imidazole ring and the quinone carbonyl oxygen O1, an in-plane hydrogen bond angle $\alpha = 0°$, an out-of-plane hydrogen bond angle $\beta = 30°$, and a twist angle between SQ and imidazole rings $\varphi = 30°$ (angles α, β and φ are defined in Fig. S3) [25]. In particular, this model accounts well for the unusually small value of the isotropic hfcc to the three equivalent methyl protons substituting the $MSK_D$ aromatic ring (i.e. $A_{iso} \sim 5.5$ MHz).

**Table 2**

Comparison between principal values of the g-tensor and $^{1}$H hyperfine coupling tensors of $DMSK_D$ determined from analysis of HYSCORE spectra, or calculated by DFT methods using the Im-DMSK model with a C2C3CβCγ dihedral angle γ = 10°. Proton numbering is according to molecular positions given in Fig. 1. Principal values of the axial hyperfine tensors are defined as [$A_{iso}$-T, $A_{iso}$-T, $A_{iso}$+2T] using the values given in Table S1, unless otherwise specified, and the corresponding signs of $A_{iso}$ and T are selected according to DFT calculations.

| | | Experimental | Calculated |
|---|---|---|---|
| *g-tensor principal values* | | | |
| | | 2.0061, 2.0050, 2.0023 | 2.0064, 2.0051, 2.0022 |
| *$^{1}$H hyperfine coupling tensors [MHz]* | | | |
| Proton numbering | Assignment | $A_{iso}$<br>[$A_{\perp}$, $A_{\perp}$, $A_{//}$] | $A_{iso}$<br>[$A_X$, $A_Y$, $A_Z$] |
| H2 | $H_B$ | -5.4[1]<br>[-8.4, -8.4, 0.6] [1,2] | -5.4<br>[-7.9, -8.4, -0.1] |
| $H_{\beta\text{-}CH2}$ | $H_D$ | 11.5[1]<br>[9.4, 9.4, 15.7] [1,3] | 12.1<br>[11.1, 15.6, 9.7] |
| | $H_E$ | 16.0[1]<br>[14.0, 14.0, 20.1] [1,3] | 17.8<br>[16.8, 15.7, 21.0] |
| $H_\gamma$ | $H_A$ | -1.1<br>[-3.0, -3.0, 2.7] | 0.2<br>[-0.4, -0.8, 1.8] |
| H5 | | | -0.4<br>[2.3, -2.3, -1.1] |
| H6 | | | -2.6<br>[-3.2, -4.3, -0.3] |
| H7 | | | -1.6<br>[-2.3, -2.8, 0.2] |
| H8 | | | -1.3<br>[-1.5, -3.1, 0.7] |

[1] Refined from simulations of HYSCORE spectra, or/and of X- and Q-band EPR spectra

[2] Simulations performed with Euler angles between the g- and the hfi tensors optimized to (60°, 90°, 0°)

[3] Simulations performed with Euler angles between the g- and the hfi tensors optimized to (75°, 90°, 0°)

Therefore, assuming a similar binding mode for $DMSK_{D\ and}$ $MSK_D$, the redistribution of the spin density in the ring-localized SOMO of the strongly asymmetrically bound DMSK with respect to a symmetrical hydrogen bonding situation results in its increase at carbon C3 to which the $CH_2$ group is attached (Fig. 7). This is hence expected to lead to a concomitant increase of the isotropic hfcc $A_{iso\ \beta\text{-}H}$ of these protons, according to the McLachlan formula:

$$A_{iso\ \beta\text{-}H} = (B_0 + B_1 \cos^2\theta)\ \rho_{C3}^{\pi} \quad \text{(Eq. 2)}$$

$\rho_{C3}^{\pi}$ is the spin density on carbon C3, $\theta$ is the angle between the CH bond and the axis of the $p_z$ carbon orbital both projected in a plane orthogonal to the Cα-Cβ bond (Fig. 8), $B_0$ is a constant that is close to zero, and $B_1$ is also a constant with a value in the range [120 – 212] MHz [45].

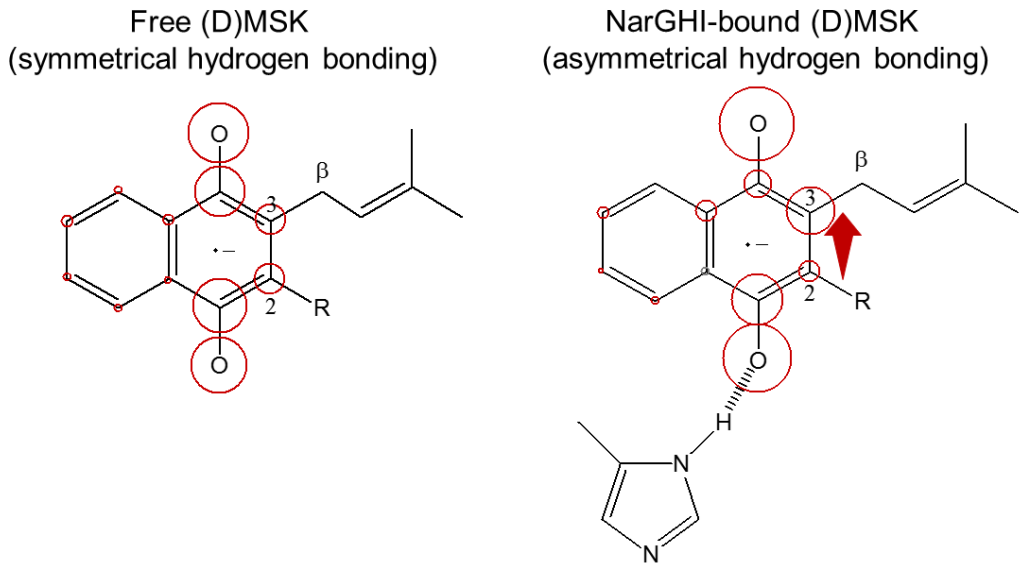


**Fig. 7**. Comparison of electronic spin density distribution between symmetrically hydrogen-bond (e.g. free) (D)MSK (left) and asymmetrically hydrogen-bond (e.g. NarGHI-bound) (D)MSK (right), with truncated isoprenyl chain. Spin density populations are represented by red circles whose radius is proportional to the spin density carried by the atom at the center of the circle (cut off = 0.01). The red arrow emphasizes the shift of the spin density from C2 to C3 due to the asymmetric $(D)MSK_D$ binding mode. H-bond partners are omitted on the left diagram. R = H (DMSK) or $CH_3$ (MSK).

Further, the nature of the substituent at the C2 carbon atom has been shown to be a crucial factor determining the θ value for semiquinones solubilized in various solvents [2, 46, 47]. In the lowest energy conformation of quinones with methyl-substituted C2 carbon (referred to as type I quinones, see Fig. 1) like MK, PhQ and UQ, the two β-$CH_2$ protons have $A_{iso\ \beta\text{-}CH2}$ values ~ 1-4 MHz, corresponding to ($\theta_1$, $\theta_2$) ~ (+60°, -60°) or ~ (+120°, -120°) [46, 48, 49] (Figure 8A and B). This translates into a C2C3CβCγ dihedral angle γ for the first isoprenyl unit relative to the quinone ring of ~ 90° or 270°, respectively, leading to a perpendicular head-to-tail orientation [2]. In contrast, type II quinones with proton-substituted C2 carbon like plastoquinones exhibit larger β-$CH_2$ couplings (e.g. $A_{iso\ \beta\text{-}CH2}$ ~ 7.0 MHz for PQ-9 in 2-propanol), corresponding to ($\theta_1$, $\theta_2$) ~ (+30°, +150°) or (-30°, -150°) for these two protons (Figure 8C and D) [2, 50-52]. The corresponding C2C3CβCγ dihedral angle γ is then 0° or 180°, respectively, placing the isoprenyl chain in the plane of the quinone ring while minimizing steric repulsions between the carbonyl oxygen and the Cγ substituents. These conclusions have been further substantiated by DFT calculations [47] and molecular dynamics simulations on PQ and UQ radical anion models [53, 54] showing that the presence or absence of the methyl group at the C2 carbon is indeed a crucial factor for determining the rotational arrangements of the quinones.

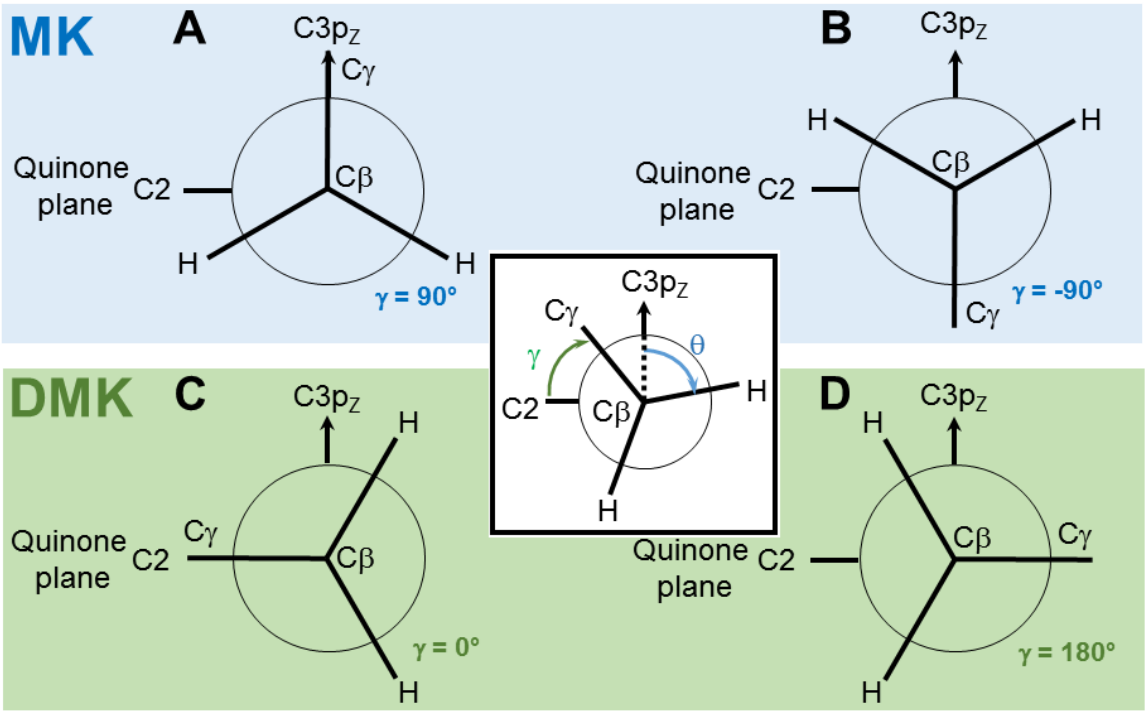


**Fig. 8.** Schematic conformation of the β-$CH_2$ protons and of the isoprenyl side chain relative to the ring for free (unbound) type I (e.g. MK) (A, B) and type II (e.g. DMK) (C, D) quinones.

Newman projections along the Cβ-C3 axis are shown. The inset shows the definitions of angles θ and γ used in the text. θ angles for the two β-$CH_2$ protons are ±120° (A), and ±60° (B), 30° and 150° (C), -30° and -150° (D).

Based on these previous works and given that DMSK is a type II quinone, we assigned $H_D$ and $H_E$ to the two β-$CH_2$ protons of the highly asymmetrically bound $DMSK_D$ side chain with an orientation suitable to generate large hyperfine coupling constants for these protons. In addition, this orientation is predicted to differ from that of $MSK_D$, explaining the apparent differences in the magnitude of the $CH_2$ hf couplings between $MSK_D$ and $DMSK_D$ inferred from analysis of their respective $^1H$ HYSCORE spectra. To further support this assignment and compare the conformation of the $DMSK_D$ and $MSK_D$ side chain relative to the quinone ring, isotropic β-$CH_2$ hfccs were computed for all possible θ values for DMSK (Fig. 9A) and MSK (Figure 9B) using the Im-DMSK and Im-MSK models, respectively. These orientations were explored through a systematic variation of the C2C3CβCγ dihedral angle γ from -180° to 180°, in 5° or 10° step. At first, it can be noticed that $A_{iso\ \beta\text{-}CH_2}$ values as high as ~20 MHz are calculated using these models, supporting the assignment of $H_D$ and $H_E$ to the two β-$CH_2$ protons of $DMSK_D$. Further, comparison between calculated β-$CH_2$ isotropic hfccs and corresponding experimental values for $H_D$ and $H_E$ (i.e. $A_{iso}$ ($H_D$) ~ 12 MHz and $A_{iso}$ ($H_E$) ~ 16 MHz) determined from spectral analysis reveals that the best agreement is found for γ values close to ± 10° (Fig. 9A). This indicates that the isoprenyl CβCγ bond of the $DMSK_D$ side chain is nearly coplanar to the aromatic ring (Fig. 10A).

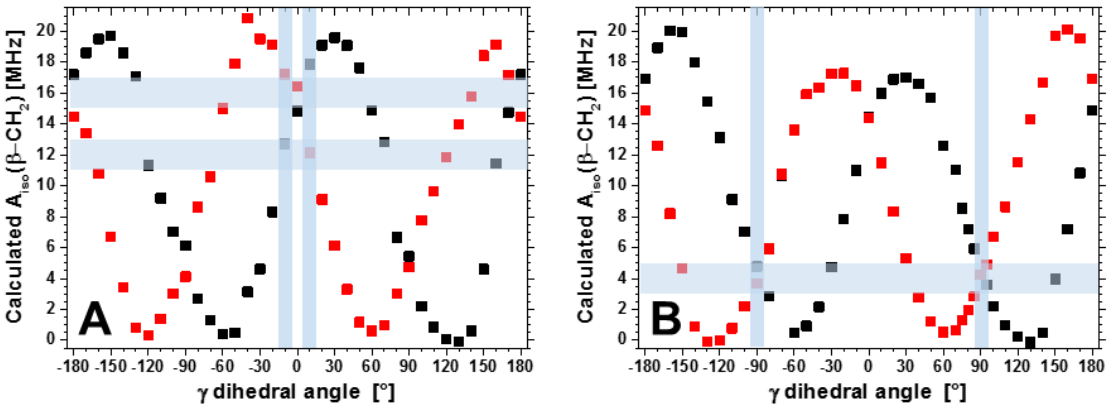


**Fig. 9.** Influence of the C2C3CβCγ dihedral angle γ on the isotropic hyperfine coupling constant $A_{iso\ \beta\text{-}CH}$ of the two β-$CH_2$ protons (red and black squares, respectively) in the Im-DMSK model (A) and Im-MSK model (B). Light blue horizontal bars show the values

consistent with HYSCORE data while light blue vertical bars show the corresponding ranges of γ values where calculated hfccs best agree with experimental data.

The principal values of the hfi tensors for non-exchangeable protons coupled to DMSK calculated using the Im-DMSK model with γ ~ +10° are reported in Table 2 where they are compared to the axially symmetric hfi tensors determined for protons $H_{A,}$ $H_{B,}$ $H_D$ and $H_E$. The calculated isotropic hfcc for the C2 α-proton H2 ($A_{iso}$ ~ -5.4 MHz) is in very good agreement with the value $A_{iso}$ ($H_B$) ~ -5.4 MHz inferred from the simulation of EPR and HYSCORE spectra (Table 2). Therefore, $H_B$ is assigned to the $DMSK_D$ C2 substituting α-proton H2. Notably, its $|A_{iso}|$ value is similar to that determined for the three equivalent methyl protons on the $MSK_D$ ring, i.e. $A_{iso}$ ~ 5.5 MHz [26]. This provides further support for the similar asymmetric binding mode of $DMSK_D$ and $MSK_D$ to *Ec*NarGHI.

Eventually, the calculated $A_{iso}$ values for the other DMSK ring protons as well as that of the γ-proton of the side-chain lie in the range [0.2 – 2.6] MHz (Table 2), the largest coupling being due to the C6 substituting proton H6. $|A_{iso}|$ values ~ 1.0 MHz determined for $H_A$ lie within this range, indicating that several protons contribute to the observed 1-1' cross peaks and that $H_A$ cannot be attributed to a single proton.

*3.6. The conformations of the $DMSK_D$ and $MSK_D$ isoprenyl chains relative to the quinone head differ by ca. 90°.*

Examination of calculated β-$CH_2$ isotropic hfccs for $MSK_D$ indicates that out-of-plane conformations with γ = ±90° (±5°) best account for our spectroscopic data on $MSK_D$ [26]. Indeed, these two situations lead to calculated $A_{iso}$ β-$CH_2$ values ~ 4-4.6 MHz for the two protons using the Im-MSK model (Fig. 9B). These are consistent with $MSK_D$ HYSCORE spectra in which no proton resonance with hfcc > 5 MHz is detected other than those clearly assigned to the methyl protons and to the exchangeable proton discussed above [26].

Beside, hfccs of 3 MHz and 1.5 MHz were resolved in $^1$H ENDOR spectra of MSK dissolved in 2-propanol and assigned to the β-$CH_2$ protons [55]. The magnitude of these couplings was shown to be indicative of the perpendicular head-to-tail orientation of the menaquinone radical anion in solution [47]. Therefore, the conformation of the $MSK_D$ side chain appears to be similar to that of the unbound species i.e. MSK in solution. Finally, the in-plane conformation of the isoprenyl chain relative to the semiquinone head of $DMSK_D$ differs from that of $MSK_D$ by ca. 90° (Fig. 10).

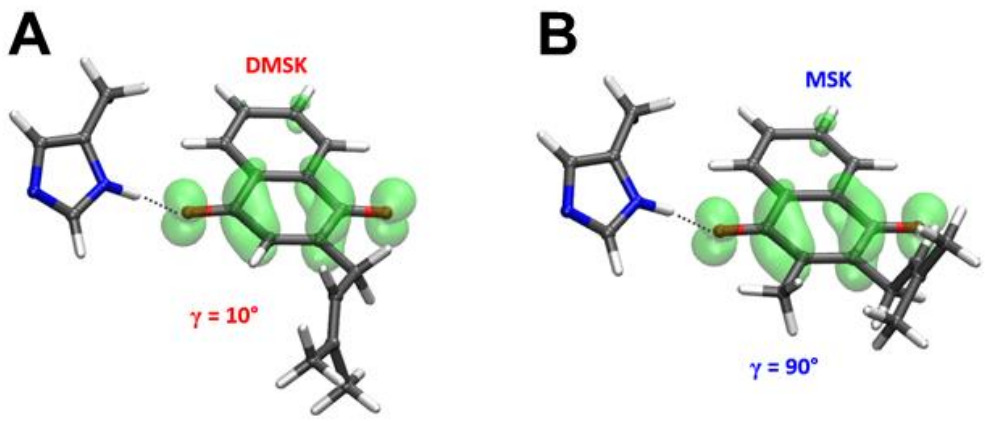


**Fig. 10.** Proposed conformations for $DMSK_D$ (A) and $MSK_D$ (B) inferred from this work. Stick representations using the Im-MSK and Im-DMSK models are shown together with the distribution of the electron spin density over the semiquinone rings (cut off = 0.003). C2C3CβCγ dihedral angle γ is 10° (A) or 90° (B).

*3.7. The protein environment in the NarGHI $Q_D$ site finely tunes the side chain orientation of the accommodated demethylmenaquinone.*

Despite their simplicity, the Im-(D)MSK models account well for the EPR spectroscopic data collected on $MSK_D$ and $DMSK_D$ without relying on any protein constraint on the side chain of the modeled quinones. In Fig. 11, the computed potential energy curves for rotation about the C3Cβ bond are compared for the Im-MSK and the Im-DMSK models. For the Im-MSK model, the potential displays two well-defined single minima at C2C3CβCγ dihedral angles γ ~ +90° and -100° as expected for type I quinones (Fig. 11, red squares). These orientations match with those determined above for $MSK_D$, indicating that the protein environment has no significant influence on the orientation of the head-to-tail orientation of the bound menasemiquinone. The two highest energy conformations arise from steric repulsion between the Cγ substituents and the C2 methyl group protons (γ ~ 0°) or O4 (γ ~ ±180°) and lead to a calculated energy barrier of ~ 5.3-5.5 kcal/mol. This barrier agrees very well with the 5-7 kcal/mol estimate obtained from linewidth effects in β-proton EPR measurements on vitamin K1 anion radicals [46].

The rotational energy plot for the Im-DMSK model in which the quinone C2 methyl group is substituted by a hydrogen atom exhibits three minima at angles γ ~ -100°, ~ 20° and ~ 110° with a low barrier ~ 1.6 $kcal.mol^{-1}$, between these three nearly perpendicular orientations (Fig. 11, black squares). Energy differences between these minima do not exceed

0.6 kcal.mol$^{-1}$, indicating that in the absence of protein constraints on the quinone side chain, DMSK can easily oscillate between these three energetically nearly equivalent conformations, leading most likely the quinone moiety to perform a wagging motion in solution, as proposed for free plastoquinones [47]. In contrast, our $^{1}$H hfc measurements show that the DMSK$_D$ aromatic ring and the isoprenyl CβCγ bond of the side chain are nearly coplanar, a situation corresponding closely to the calculated secondary energy minimum at γ ~ 20° using the Im-DMSK model. This suggests that the protein environment in the *Ec*NarGHI $Q_D$ site finely tunes the conformation of the DMSK side chain, selecting one of the three low energy conformers found in the absence of protein constraints on the side chain. Eventually, the *Ec*NarGHI $Q_D$ site appears to be able to accommodate various types of naphthoquinones with markedly different head-to-tail orientations corresponding most likely to one of the lowest energy conformations of their native semiquinones in solution.

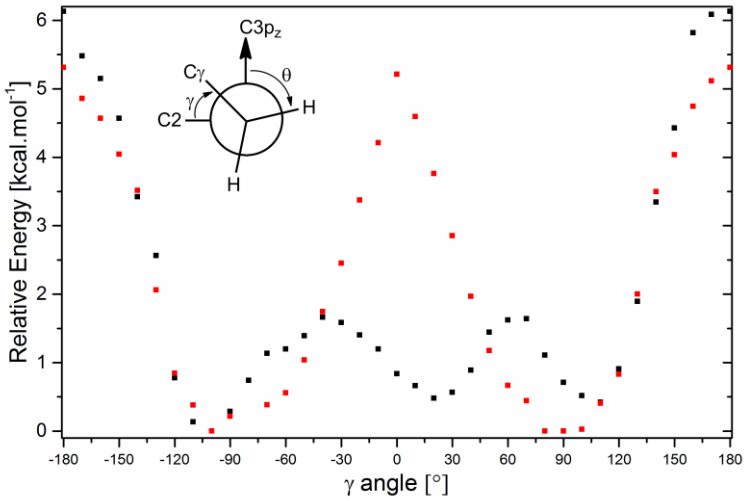


**Fig. 11** Head-to-tail rotational energy plot (kcal/mol) of the Im-MSK (red squares) and Im-DMSK (black squares) models. The insert shows the Newman projection of quinone models along the C3-Cβ axis and the definition of θ and γ angles.

*3.8. Role of the protein environment in tuning the head-to-tail orientation of the bound (semi)quinones.*

The present work shows that the protein environment in the *Ec*NarGHI $Q_D$ site can have a significant influence on the accessible conformation of the first isoprenoid unit of the side chain of the bound quinone. This property can be discussed in light of previous spectroscopic and structural studies on the well-studied primary electron acceptor $Q_A$ in bRC

or in plant photosystem II (PSII). Using temperature-dependent special TRIPLE experiments in $^2H_2O$-exchanged sample, the spectral contributions of two distinct β-$CH_2$ protons coupled to the reduced plastosemiquinone $Q_A^-$ generated in PSII could be distinguished [2]. Comparison with corresponding data obtained on free PSQ-9 in solution led to the proposal that the conformation of the PSQ isoprenyl chain at Cβ relative to the aromatic ring is conserved upon binding to PSII. Further, on the basis of comparison with available hf data obtained on type I (i.e. with a $CH_3$ group at C2) and type II semiquinone anions in solution together with analysis of the dihedral angle γ of the type I menaquinone or ubiquinone bound to the $Q_A$ site of different bacterial RCs (bRCs), it has been proposed that this angle for type II plastoquinone in the $Q_A$ site of higher plant PSII differs from that of MK or UQ in bRC by ca. 90°. Interestingly, quinone replacement experiments have highlighted a high specificity of the $Q_A$ site in PSII and in bRC for their respective endogenous quinone [56, 57] and this has been proposed to arise from the evolution of different reaction center protein structures surrounding the isoprenyl/quinone head junction to accommodate the favoured low energy conformers of type I and type II semiquinones [2].

However, it is worth to mention that the conformations of the plastoquinone side-chain within the PSII $Q_A$ site resolved in the available X-ray crystal structures appear very diverse, ranging from an almost in-plane conformation with γ = -10° in the PSII from *Thermosynechococcus elongatus* (pdb code 5MX2) [58], to a perpendicular head-to-tail conformation with γ = 88°- 89° in that from *Pisum sativum* (pdb code 5XNL) [59], via intermediate situations with γ angles in the range of 32° to 70° in the PSII from *Thermosynechococcus vulcanus* (pdb code 5B66) [60] or *Thermosynechococcus elongatus*. In line with our results on the NarGHI $Q_D$ site, this shows that the protein environment can tune the conformation of the bound quinones. In the case of $MSK_D$, the steric interactions between the isoprenyl chain and the substituting methyl group on C2 are stronger than the constraints due to the protein environment, and the perpendicular orientation of the isoprenyl chain with respect to the aromatic ring is maintained. In contrast, in $DMSK_D$, the steric interactions of the isoprenyl chain with the C2 substituent are weaker and the protein constraints are sufficient to enable a conformation selection leading to an isoprenyl chain parallel to the ring. Such an influence of the protein surrounding on the quinone conformation could play a role in either optimizing enzyme functioning and/or in tuning the specificity of a given Q site towards quinones [2].

*3.9. Implications of the presence/absence of a ring methyl group on the structure and function of Q sites.*

While it has been shown *in vivo* that several bioenergetics complexes can react with both MK and DMK, e.g. *E. coli* cytochrome $bo_3$ and cytochrome *bd* [61], detailed molecular investigations aimed at comparing the binding mode and the functional properties of these two different quinones bound to the same Q site are still lacking. In a previous study on PSI, it has been shown that the inactivation of the gene (i.e. *menG*) responsible for transferring the methyl group to 2-phytyl-1,4-naphthoquinone in the biosynthetic pathway of phylloquinone (a type I quinone, Fig. 1) results in the incorporation of a 2-phytyl-1,4-naphthoquinone (i.e. a type II quinone) into the $A_1$ site normally occupied by a phylloquinone [62]. Continuous wave and time-resolved EPR measurements have shown that the corresponding light-induced semiquinone radical has the same orientation as phylloquinone and shows the same distance to the $P700^+$ primary donor. In addition, the internal electron transfer is affected in a way qualitatively consistent with the expected change in midpoint potential of the bound quinones. Notably, no β-$CH_2$ proton coupling to the $A_1$ semiquinone has been identified by EPR methods. This is most likely due to some distribution of the corresponding hfccs consecutive to small variations of the γ-angle [49, 63] and precluded any detailed analysis of side chain conformational changes of semiquinones bound to the PSI $A_1$-site upon removal of the phylloquinone ring methyl group.

In the case of *Ec*NarGHI, in addition to the ~ 90° rotation of the quinone side chain relative to the ring in the $Q_D$ site when going from MSK to DMSK, substitution of the C2 ring methyl group by a hydrogen atom on the naphthoquinone ring is associated to a downshift of the two-electron midpoint potential of the NarGHI-bound DMK by ~ 30 mV with respect to the unbound species. This phenomenon was neither observed for $MSK_D$ nor for $USQ_D$ [19] and reveals a ~10 fold tighter binding of DMK than $DMKH_2$ to the $Q_D$ site. Notably, varying the orientation of the quinone side-chain in our simple Im-(D)MSK model does not significantly affect the semiquinone electronic structure. This indicates that this orientation itself does not significantly influence the quinone redox properties, in contrast to that of the ubiquinone methoxy groups [64]. Therefore, the origin of this shift is most likely due to protein environment effects that have to be considered to elucidate the factors that fine-tune the $DMSK_D$ side chain conformation and redox properties. This will require further detailed experimental and theoretical investigations.

## 4. Conclusions

*Ec*NarGHI $Q_D$ site stabilizes the semiquinone radical of MK and DMK via a similar short H-bond between the semiquinone O1 oxygen and the imidazole Nδ of the heme $b_D$ axial ligand His66 while essentially maintaining the markedly different side-chain orientations of the unbound species. This adaptability of the *Ec*NarGHI $Q_D$ site could contribute to the metabolic flexibility of NarGHI, a key player in the energy metabolism of the bacterium upon variations of the quinone content of the Q-pool consecutive to variations of the *E. coli* niche. In mammalian intestines, this niche indeed alternates between microaerobic and anaerobic, conditions in which electron flow to NarGHI via MK and DMK contributes a major colonization advantage [65, 66].


## Acknowledgements

This work was supported by the A*MIDEX project MicrobioE funded by the "Investissements d'Avenir" French Government program (ANR-11-IDEX-0001-02), the CNRS "Mission pour l'interdisciplinarité" program (project "Instrumentations aux limites"), and the French EPR network (RENARD, IR3443). DFT calculations were performed by using computing resources from the "Centre Régional de Compétences en Modélisation Moléculaire" (CRCMM, Marseille). We thank Dr. Emilien Etienne and Dr. Guillaume Gerbaud for their assistance in the use of the Aix-Marseille EPR facility. MSE was supported by a PhD fellowship from the Lebanese Government and by the A*MIDEX programme for Aix-Marseille technological platforms. JR was supported by a CNRS/Région Provence-Alpes-Côte d'Azur PhD fellowship.


## Appendix A. Supplementary data

Supplementary data to this article available.

## References


[1] M.D. Collins, D. Jones, Distribution of isoprenoid quinone structural types in bacteria and their taxonomic implication, Microbiol. Rev. 45 (1981) 316-354.
[2] M. Zheng, G.C. Dismukes, The conformation of the isoprenyl chain relative to the semiquinone head in the primary electron acceptor (QA) of higher plant PSII (plastosemiquinone) differs from that in bacterial reaction centers (ubisemiquinone or menasemiquinone) by ca. 90 degrees, Biochemistry 35 (1996) 8955-8963.
[3] E. Maklashina, G. Cecchini, S.A. Dikanov, Defining a direction: Electron transfer and catalysis in *Escherichia coli* complex II enzymes, Biochim. Biophys. Acta 1827 (2013) 668-678.

[4] N. Srinivasan, J.H. Golbeck, Protein-cofactor interactions in bioenergetic complexes: the role of the A1A and A1B phylloquinones in Photosystem I, Biochim. Biophys. Acta 1787 (2009) 1057-1088.
[5] S. Grimaldi, B. Schoepp-Cothenet, P. Ceccaldi, B. Guigliarelli, A. Magalon, The prokaryotic Mo/W-*bis*PGD enzymes family: a catalytic workhorse in bioenergetic, Biochim. Biophys. Acta 1827 (2013) 1048-1085.
[6] B. Soballe, R.K. Poole, Microbial ubiquinones: multiple roles in respiration, gene regulation and oxidative stress management, Microbiology 145 (1999) 1817-1830.
[7] B.J. Wallace, I.G. Young, Role of quinones in electron transport to oxygen and nitrate in *Escherichia coli*. Studies with a ubiA- menA- double quinone mutant, Biochim. Biophys. Acta 461 (1977) 84-100.
[8] M.G. Bertero, R.A. Rothery, N. Boroumand, M. Palak, F. Blasco, N. Ginet, J.H. Weiner, N.C. Strynadka, Structural and biochemical characterization of a quinol binding site of *Escherichia coli* nitrate reductase A, J. Biol. Chem. 280 (2005) 14836-14843.
[9] F. Blasco, B. Guigliarelli, A. Magalon, M. Asso, G. Giordano, R.A. Rothery, The coordination and function of the redox centres of the membrane-bound nitrate reductases, Cell. Mol. Life Sci. 58 (2001) 179-193.
[10] M.G. Bertero, R.A. Rothery, M. Palak, C. Hou, D. Lim, F. Blasco, J.H. Weiner, N.C. Strynadka, Insights into the respiratory electron transfer pathway from the structure of nitrate reductase A, Nat. Struct. Biol. 10 (2003) 681-687.
[11] J. Rendon, F. Biaso, P. Ceccaldi, R. Toci, F. Seduk, A. Magalon, B. Guigliarelli, S. Grimaldi, Elucidating the Structures of the Low- and High-pH Mo(V) Species in Respiratory Nitrate Reductase: A combined EPR, N-14,N-15 HYSCORE, and DFT Study, Inorg. Chem. 56 (2017) 4422-4434.
[12] R.A. Rothery, M.G. Bertero, R. Cammack, M. Palak, F. Blasco, N.C. Strynadka, J.H. Weiner, The catalytic subunit of *Escherichia coli* nitrate reductase A contains a novel [4Fe-4S] cluster with a high-spin ground state, Biochemistry 43 (2004) 5324-5333.
[13] P. Lanciano, A. Savoyant, S. Grimaldi, A. Magalon, B. Guigliarelli, P. Bertrand, New method for the spin quantitation of $[4Fe\text{-}4S]^{+}$ clusters with S = 3/2. Application to the FS0 center of the NarGHI nitrate reductase from *Escherichia coli*, J. Phys. Chem. B 111 (2007) 13632-13637.
[14] B. Guigliarelli, A. Magalon, M. Asso, P. Bertrand, C. Frixon, G. Giordano, F. Blasco, Complete coordination of the four Fe-S centers of the beta subunit from *Escherichia coli* nitrate reductase. Physiological, biochemical, and EPR characterization of site-directed mutants lacking the highest or lowest potential [4Fe-4S] clusters, Biochemistry 35 (1996) 4828-4836.
[15] R.A. Rothery, F. Blasco, A. Magalon, J.H. Weiner, The diheme cytochrome *b* subunit (NarI) of *Escherichia coli* nitrate reductase A (NarGHI): structure, function, and interaction with quinols, J. Mol. Microbiol. Biotechnol. 3 (2001) 273-283.
[16] A. Magalon, D. Lemesle-Meunier, R.A. Rothery, C. Frixon, J.H. Weiner, F. Blasco, Heme axial ligation by the highly conserved His residues in helix II of cytochrome *b* (NarI) of *Escherichia coli* nitrate reductase A, J. Biol. Chem. 272 (1997) 25652-25658.
[17] U. Wissenbach, A. Kroger, G. Unden, The specific functions of menaquinone and demethylmenaquinone in anaerobic respiration with fumarate, dimethylsulfoxide, trimethylamine N-oxide and nitrate by *Escherichia coli*, Arch. Microbiol. 154 (1990) 60-66.
[18] U. Wissenbach, D. Ternes, G. Unden, An *Escherichia coli* mutant containing only demethylmenaquinone, but no menaquinone: effects on fumarate, dimethylsulfoxide, trimethylamine N-oxide and nitrate respiration, Arch. Microbiol. 158 (1992) 68-73.
[19] J. Rendon, E. Pilet, Z. Fahs, F. Seduk, L. Sylvi, M.H. Chehade, F. Pierrel, B. Guigliarelli, A. Magalon, S. Grimaldi, Demethylmenaquinol is a substrate of *Escherichia coli* nitrate

reductase A (NarGHI) and forms a stable semiquinone intermediate at the NarGHI quinol oxidation site, Biochim. Biophys. Acta 1847 (2015) 739-747.
[20] R. Hollander, Correlation of the function of demethylmenaquinone in bacterial electron transport with its redox potential, FEBS Lett. 72 (1976) 98-100.
[21] P. Infossi, E. Lojou, J.-P. Chauvin, G. Herbette, M. Brugna, M.-T. Giudici-Orticoni, *Aquifex aeolicus* membrane hydrogenase for hydrogen biooxidation: Role of lipids and physiological partners in enzyme stability and activity, Int. J. Hydrog. Energy 35 (2010) 10778-10789.
[22] R. Arias-Cartin, S. Lyubenova, P. Ceccaldi, T. Prisner, A. Magalon, B. Guigliarelli, S. Grimaldi, HYSCORE evidence that endogenous mena- and ubisemiquinone bind at the same Q site ($Q_D$) of *Escherichia coli* nitrate reductase A, J. Am. Chem. Soc. 132 (2010) 5942-5943.
[23] S. Grimaldi, R. Arias Cartin, P. Lanciano, S. Lyubenova, B. Endeward, T.F. Prisner, A. Magalon, B. Guigliarelli, Direct evidence for nitrogen ligation to the high-stability semiquinone intermediate in *Escherichia coli* nitrate reductase A, J. Biol. Chem. 285 (2010) 179-187.
[24] P. Lanciano, A. Magalon, P. Bertrand, B. Guigliarelli, S. Grimaldi, High-stability semiquinone intermediate in nitrate reductase A (NarGHI) from *Escherichia coli* is located in a quinol oxidation site close to heme $b_D$, Biochemistry 46 (2007) 5323-5329.
[25] M. Seif Eddine, F. Biaso, R. Arias-Cartin, E. Pilet, J. Rendon, S. Lyubenova, F. Seduk, B. Guigliarelli, A. Magalon, S. Grimaldi, Probing the menasemiquinone binding mode to nitrate reductase A by selective 2H & 15N labelling, HYSCORE spectroscopy and DFT modeling, ChemPhysChem 18 (2017) 1-12.
[26] S. Grimaldi, R. Arias-Cartin, P. Lanciano, S. Lyubenova, R. Szenes, B. Endeward, T.F. Prisner, B. Guigliarelli, A. Magalon, Determination of the proton environment of high stability Menasemiquinone intermediate in *Escherichia coli* nitrate reductase A by pulsed EPR, J. Biol. Chem. 287 (2012) 4662-4670.
[27] S. Grimaldi, P. Lanciano, P. Bertrand, F. Blasco, B. Guigliarelli, Evidence for an EPR-detectable semiquinone intermediate stabilized in the membrane-bound subunit NarI of nitrate reductase A (NarGHI) from *Escherichia coli*, Biochemistry 44 (2005) 1300-1308.
[28] L.C. Potter, P. Millington, L. Griffiths, G.H. Thomas, J.A. Cole, Competition between *Escherichia coli* strains expressing either a periplasmic or a membrane-bound nitrate reductase: does Nap confer a selective advantage during nitrate-limited growth?, Biochem. J. 344 (1999) 77-84.
[29] S. Stoll, R.D. Britt, General and efficient simulation of pulse EPR spectra, Phys. Chem. Chem. Phys. 11 (2009) 6614-6625.
[30] S.A. Dikanov, M.K. Bowman, Cross-peak lineshape of two-dimensional ESEEM spectra in disordered S = 1/2, I = 1/2 spin systems, J. Magn. Reson. A 116 (1995) 125-128.
[31] F. Neese, The ORCA program system, Wiley Interdisciplinary Reviews-Computational Molecular Science 2 (2012) 73-78.
[32] A. Schafer, H. Horn, R. Ahlrichs, Fully optimized contracted Gaussian-basis sets for atoms Li to Kr, J. Chem. Phys. 97 (1992) 2571-2577.
[33] A. Schafer, C. Huber, R. Ahlrichs, Fully optimized contracted Gaussian basis sets of triple zeta valence quality for atoms Li to Kr, J. Chem. Phys. 100 (1994) 5829-5835.
[34] F. Neese, An improvement of the resolution of the identity approximation for the formation of the Coulomb matrix, J. Comput. Chem. 24 (2003) 1740-1747.
[35] V. Barone, Structure, Magnetic Properties and Reactivities of Open-Shell Species from Density Functional and Self-consistent Hybrid Methods, in: D.P. Chong (Ed.) Recent Advances in Density Functional Methods, World Scientific, 1995, pp. 287-334.

[36] A. Klamt, G. Schuurmann, COSMO - A new approach to dielectric screening in solvents with explicit expressions for the screening energy and its gradient, J. Chem. Soc. Perkin Trans. 2 (1993) 799-805.
[37] S.A. Dikanov, Y.D. Tsvetkov, Electron spin echo envelope modulation (ESEEM) spectroscopy, CRC Press, Boca Raton, 1992.
[38] S.A. Dikanov, R.I. Samoilova, D.R. Kolling, J.T. Holland, A.R. Crofts, Hydrogen bonds involved in binding the $Q_i$-site semiquinone in the $bc_1$ complex, identified through deuterium exchange using pulsed EPR, J. Biol. Chem. 279 (2004) 15814-15823.
[39] A. Poppl, R. Bottcher, Cross peak intensities in two-dimensional four-pulse electron spin echo modulation spectra of deuteriums in single crystals, Chem. Phys. 221 (1997) 53-66.
[40] A. Poppl, M. Hartmann, W. Bohlmann, R. Bottcher, Coordination geometry of the copper-pyridine complex in frozen solution as studied by proton and deuterium two-dimensional hyperfine sublevel correlation electron spin resonance spectroscopy, J. Phys. Chem. A 102 (1998) 3599-3606.
[41] S. Sinnecker, E. Reijerse, F. Neese, W. Lubitz, Hydrogen bond geometries from electron paramagnetic resonance and electron-nuclear double resonance parameters: density functional study of quinone radical anion-solvent interactions, J. Am. Chem. Soc. 126 (2004) 3280-3290.
[42] M. Flores, R. Isaacson, E. Abresch, R. Calvo, W. Lubitz, G. Feher, Protein-cofactor interactions in bacterial reaction centers from Rhodobacter sphaeroides R-26: II. Geometry of the hydrogen bonds to the primary quinone formula by 1H and 2H ENDOR spectroscopy, Biophys. J. 92 (2007) 671-682.
[43] S.A. Dikanov, Resolving protein-semiquinone interactions by two-dimensional ESEEM spectroscopy, Electron Paramagnetic Resonance v.23, RSC Publishing, 2013, pp. 103-179.
[44] W. Lubitz, G. Feher, The primary and secondary acceptors in bacterial photosynthesis. III. Characterization of the quinone radicals $Q_A^{-\cdot}$ and $Q_B^{-\cdot}$ by EPR and ENDOR, Appl. Magn. Reson. 17 (1999) 1-48.
[45] H.M. McConnell, Indirect Hyperfine Interactions in the Paramagnetic Resonance Spectra of Aromatic Free Radicals, J. Chem. Phys. 24 (1956) 764-766.
[46] M.R. Das, H.D. Connor, D.S. Leniart, J.H. Freed, An Electron Nuclear Double Resonance and Electron Spin Resonance Study of Semiquinones Related to Vitamins K and E, J. Am. Chem. Soc. 92 (1970) 2258-2268.
[47] F. Himo, G.T. Babcock, L.A. Eriksson, Conformational analysis of quinone anion radicals in photosystem II and photosynthetic bacteria, J. Phys. Chem. A 103 (1999) 3745-3749.
[48] G. Feher, R.A. Isaacson, M.Y. Okamura, W. Lubitz, ENDOR of Semiquinones in RCs from *Rhodopseudomonas sphaeroides*, in: M.E. Michel-Beyerle (Ed.) Antennas and Reaction Centers of Photosynthetic Bacteria, Springer-Verlag, Place Published, 1985, pp. 174-189.
[49] C. Teutloff, R. Bittl, W. Lubitz, Pulse ENDOR Studies on the Radical Pair P700+.A1.- and the Photoaccumulated Quinone Acceptor A1.- of Photosystem I, Appl. Magn. Reson. 26 (2004) 5-21.
[50] F. MacMillan, F. Lendzian, W. Lubitz, EPR and ENDOR characterization of semiquinone anion radicals related to photosynthesis, Magn. Reson. Chem. 33 (1995) S81-S93.
[51] F. MacMillan, F. Lendzian, G. Renger, W. Lubitz, EPR and ENDOR investigation of the primary electron acceptor radical anion $Q_A^{\cdot -}$ in iron-depleted photosystem II membrane fragments, Biochemistry 34 (1995) 8144-8156.
[52] S.E. Rigby, P. Heathcote, M.C. Evans, J.H. Nugent, ENDOR and special TRIPLE resonance spectroscopy of QA.- of photosystem 2, Biochemistry 34 (1995) 12075-12081.

[53] J.A. Nilsson, L.A. Eriksson, A. Laaksonen, Molecular dynamics simulations of plastoquinone in solution, Mol. Phys. 99 (2001) 247-253.
[54] J.A. Nilsson, A. Lyubartsev, L.A. Eriksson, A. Laaksonen, Molecular dynamics simulations of ubiquinone; a survey over torsional potentials and hydrogen bonds, Mol. Phys. 99 (2001) 1795-1804.
[55] A.T. Gardiner, S.G. Zech, F. MacMillan, H. Kass, R. Bittl, E. Schlodder, F. Lendzian, W. Lubitz, Electron paramagnetic resonance studies of zinc-substituted reaction centers from *Rhodopseudomonas viridis*, Biochemistry 38 (1999) 11773-11787.
[56] M.Y. Okamura, R.A. Isaacson, G. Feher, Primary acceptor in bacterial photosynthesis: obligatory role of ubiquinone in photoactive reaction centers of *Rhodopseudomonas spheroides*, Proc. Natl. Acad. Sci. USA 72 (1975) 3491-3495.
[57] B.A. Diner, C. Devitry, J.L. Popot, Quinone-exchange in the QA binding site of photosystem II reaction center core preparations isolated from *Chlamydomonas reinhardtii*, Biochim. Biophy. Acta 934 (1988) 47-54.
[58] M. Zhang, M. Bommer, R. Chatterjee, R. Hussein, J. Yano, H. Dau, J. Kern, H. Dobbek, A. Zouni, Structural insights into the light-driven auto-assembly process of the water-oxidizing Mn4CaO5-cluster in photosystem II, Elife 6 (2017).
[59] X. Su, J. Ma, X. Wei, P. Cao, D. Zhu, W. Chang, Z. Liu, X. Zhang, M. Li, Structure and assembly mechanism of plant C2S2M2-type PSII-LHCII supercomplex, Science 357 (2017) 815-820.
[60] A. Tanaka, Y. Fukushima, N. Kamiya, Two Different Structures of the Oxygen-Evolving Complex in the Same Polypeptide Frameworks of Photosystem II, J. Am. Chem. Soc. 139 (2017) 1718-1721.
[61] P. Sharma, M.J. Teixeira de Mattos, K.J. Hellingwerf, M. Bekker, On the function of the various quinone species in *Escherichia coli*, FEBS J. 279 (2012) 3364-3373.
[62] Y. Sakuragi, B. Zybailov, G. Shen, A.D. Jones, P.R. Chitnis, A. van der Est, R. Bittl, S. Zech, D. Stehlik, J.H. Golbeck, D.A. Bryant, Insertional inactivation of the *menG* gene, encoding 2-phytyl-1,4-naphthoquinone methyltransferase of *Synechocystis* sp. PCC 6803, results in the incorporation of 2-phytyl-1,4-naphthoquinone into the A(1) site and alteration of the equilibrium constant between A(1) and F(X) in photosystem I, Biochemistry 41 (2002) 394-405.
[63] J. Niklas, B. Epel, M.L. Antonkine, S. Sinnecker, M.E. Pandelia, W. Lubitz, Electronic structure of the quinone radical anion A1*- of photosystem I investigated by advanced pulse EPR and ENDOR techniques, J. Phys. Chem. B 113 (2009) 10367-10379.
[64] A.T. Taguchi, A.J. Mattis, P.J. O'Malley, S.A. Dikanov, C.A. Wraight, Tuning cofactor redox potentials: the 2-methoxy dihedral angle generates a redox potential difference of >160 mV between the primary (Q(A)) and secondary (Q(B)) quinones of the bacterial photosynthetic reaction center, Biochemistry 52 (2013) 7164-7166.
[65] S.A. Jones, F.Z. Chowdhury, A.J. Fabich, A. Anderson, D.M. Schreiner, A.L. House, S.M. Autieri, M.P. Leatham, J.J. Lins, M. Jorgensen, P.S. Cohen, T. Conway, Respiration of *Escherichia coli* in the mouse intestine, Infect. Immun. 75 (2007) 4891-4899.
[66] S.A. Jones, T. Gibson, R.C. Maltby, F.Z. Chowdhury, V. Stewart, P.S. Cohen, T. Conway, Anaerobic respiration of *Escherichia coli* in the mouse intestine, Infect. Immun. 79 (2011) 4218-4226.